Extensive investigation of the influence of wall permeability on turbulence

Extensive investigation of the influence of wall permeability on turbulence

Y. Kuwata[a,*], K. Suga[a]

[a]*Department of Mechanical Engineering, Osaka Prefecture University, Sakai, Osaka 599-8531, Japan*

Abstract

A series of direct numerical simulations of turbulent porous-walled channel flows is performed to extensively investigate the influence of wall permeability on turbulence modification. The bulk mean Reynolds number is fixed at 3000, and porous media consisting of perforated plates are considered in the lower side of the channel. The mean-permeability Reynolds number is varied from $14 - 118$ by varying the hole size of the perforated plates. A spectral analysis reveals the presence of two characteristic perturbation modes, namely, the streamwise perturbation mode originating from the Kelvin–Helmholtz (K–H) type of instability and the spanwise perturbation mode. When the mean permeability Reynolds number is relatively low, the streamwise perturbation model by the K–H instability is dominant, and this increases the coherence of the wall-ward turbulence motion, thus resulting in considerable turbulence enhancement. However, as the mean permeability Reynolds number increases further, the streamwise perturbations tend to decrease in strength, and the streamwise elongated high- and low-speed streaky structure, the mean spacing of which is much longer than that over a smooth wall, is developed owing to the spanwise perturbation mode. In this regime, the

*corresponding author

Email address: kuwata@me.osakafu-u.ac.jp (Y. Kuwata)

turbulence enhancement effect is weakened because of an increased slippage velocity at the porous interface.
Keywords: Turbulence modelling, Rough wall turbulence, Double averaging, Second moment closure

1. Introduction

The turbulent flow over a permeable porous wall has received much attention in the past decades because many engineering and environmental flows over real surfaces are largely influenced by wall permeability, e.g., flows over the carbon paper of fuel cells, open-cell metal foams of heat exchangers, gravel beds of natural rivers, atmospheric or aquatic vegetation, and urban buildings. Many experimental and numerical studies have been focused on understanding the influence of porous walls on the interface turbulence between a free fluid and porous media (e.g., Lovera and Kennedy, 1969; Ruff and Gelhar, 1972; Ho and Gelhar, 1973; Kong and Schetz, 1982; Zippe and Graf, 1983; iménez et al., 2001; Breugem et al., 2006; White and Nepf, 2007; Nepf and Ghisalberti, 2008; Suga et al., 2010; Manes et al., 2011; Kuwata and Suga, 2016b; Rosti et al., 2018).

Based on the measurements of the skin friction factor at a porous wall previously obtained by Lovera and Kennedy (1969); Ruff and Gelhar (1972); Ho and Gelhar (1973); Kong and Schetz (1982); Zippe and Graf (1983), a consensus was reached that the friction factor over a porous wall is increased owing to the combined effects of surface roughness and porous media. Kong and Schetz (1982) examined the turbulence boundary layer flows over several types of walls including sintered metal, bonded screening, a perforated sheet,

and a sand-roughened wall and revealed that the friction factor was increased owing to porosity effects as well as roughness effects. In addition to the porosity, there are several important parameters for porous medium flows. One of the key parameters used to measure the viscous flow resistance is the permeability, and many systematic investigations have been performed to identify the influence of the wall permeability on turbulence (Ho and Gelhar, 1973; Manes et al., 2009; Suga et al., 2010; Breugem et al., 2006; Kuwata and Suga, 2016b). The permeability has been defined in the convection theory for porous medium flows proposed by Darcy (1856), who assumed the existence of a proportionality between the flow rate and pressure difference:

$$U_i = -\frac{K_{ij}}{\mu}\left(\frac{\partial P}{\partial x_j} - \rho g_i\right), \tag{1}$$

where K_{ij}, U_i, P, g_i, μ, and ρ are the permeability tensor, Darcian velocity (superficially averaged velocity), fluid-phase averaged pressure, gravitational acceleration, dynamic viscosity, and density of the fluid, respectively. It should be noted that the permeability is a second-order tensor; however, the permeability can usually be treated as a scaler value K for isotropic porous media owing to the following relation: $K = K_{11} = K_{22} = K_{33}$ and $K_{12} = K_{23} = K_{31} = 0$.

Ho and Gelhar (1973) performed hot-film anemometry measurements on turbulent boundary layer flows over a permeable wall and an impermeable rough wall, both of which had identical roughness. They found that the friction factor of the permeable wall was higher than that of the impermeable rough wall, which suggests that the wall permeability caused an increase in the friction factor. Manes et al. (2009) selected the same approach to systematically examine the influence of the wall permeability. They performed

velocity measurements in open-channel flows over an impermeable wall comprising a single layer of spheres and that over a permeable wall comprising five layers of spheres. It should be noted that the porosities of the two walls were the same, and the only difference was the wall permeability. They confirmed that the permeable wall provided a higher flow resistance than the impermeable wall and found that there was an intense transport of turbulent kinetic energy near the interface region between the clear fluid and porous medium. Using particle image velocimetry, Suga et al. (2010) systematically studied the influence of wall permeability on turbulence. They reported that, as the wall permeability increased, the wall-normal Reynolds stress was enhanced owing to the relaxation of the wall-blocking effects, thus resulting in an increase in the friction factor over the porous media. Moreover, to characterise the influence of the wall permeability on a mean velocity profile over a porous wall, they proposed correlation functions for the Kármán constant, zero-plane displacement, and equivalent roughness height as functions of the permeability Reynolds number, which is based on the friction velocity u_τ and square root of the permeability as follows:

$$Re_K = \frac{\sqrt{K}u_\tau}{\nu}. \tag{2}$$

The influence of the wall permeability was also studied via the direct numerical simulation (DNS) (iménez et al., 2001; Breugem et al., 2006; Kuwata and Suga, 2016b; Rosti et al., 2015). Not only does the DNS enable us to obtain the precise turbulence statistics over a porous wall, but the DNS can also provide high fidelity flow information of the turbulence statistics inside a porous wall that cannot be easily accessed via experimental investigations. Kuwata and Suga (2016b) performed a lattice Boltzmann DNS of

the turbulence over rough and porous walls having identical surface roughness. In contrast to the other numerical simulation studies that model the flow inside a porous wall, Kuwata and Suga (2016b) fully resolved the rough and porous geometries. They confirmed that the turbulence was enhanced by the wall permeability as well as the wall roughness, thus supporting the many experimental findings mentioned above. In addition, they confirmed the presence of a large-scale streamwise perturbation over the porous wall, resulting from a Kelvin–Helmholtz (K–H) type of instability that is initiated by the strong shear and velocity inflection. This large-scale coherent structure, also known as spanwise rollers, has been discussed in detail in the field of a vegetation canopy flow (Raupach et al., 1996; Ghisalberti and Nepf, 2002; White and Nepf, 2007; Finnigan, 2000) and also confirmed by the other numerical studies that applied drag force model inside a porous wall iménez et al. (2001); Breugem et al. (2006). Moreover, from a snapshot proper orthogonal decomposition analysis, Kuwata and Suga (2016b) found that large-scale pressure perturbations were generated over the porous wall but not over the rough wall, and the budget term analyses conducted in the same flow system by Kuwata and Suga (2016c) showed that the intensified pressure fluctuations enhanced the turbulent transport through the pressure diffusion and re-distribution processes.

Many other important numerical and experimental studies on turbulence over a porous wall can be found in the literature, and the majority of them have reached the conclusion that the higher the wall permeability becomes, the more the turbulence is enhanced. However, the permeability of a porous medium varies over a wide range depending on the structure of the porous

media: the permeability of the soil, concrete, or gravel is several orders of magnitude smaller than that of sparse vegetation or urban canopies. A porous wall with a very small permeability almost behaves like an impermeable rough wall; thus, an increase/decrease in the wall permeability does not significantly affect the turbulence. In the case of an excessively high wall permeability, the fluid flow is hardly blocked; thus, an increase/decrease in the wall permeability has a smaller influence on the turbulence as in the case of a wall having a very low permeability. Accordingly, it can be expected that the influence of the wall permeability on the turbulence is not monotonic, and the turbulence is strongly dependent on the magnitude of the wall permeability However, to the best of the authors ' knowledge, there exist no studies that include a wall with a very low permeability and one with a high permeability. For example, the ranges of the permeability Reynolds number Re_K studied thus far are as follows: $0 < \mathrm{Re}_K < 17$ in Manes et al. (2009), $0.81 < \mathrm{Re}_K < 11$ in Suga et al. (2010), $0.31 < \mathrm{Re}_K < 9.4$ in Breugem et al. (2006), $0.05 < \mathrm{Re}_K < 0.75$ in Rosti et al. (2015), and $\mathrm{Re}_K = 3.8$ in Kuwata and Suga (2016b). Accordingly, the purpose of the present study is to provide a unified view of the wall permeability effects on turbulence. We thus conduct a series of DNSs comprising turbulent flows over porous walls while varying the permeability Reynolds number roughly from 10 to 100 and while including the low-wall-permeability cases, such that a porous wall behaves as a smooth wall, and the high-wall-permeability cases, such that a porous wall hardly blocks the fluid flow. We examine the influence of the wall permeability on the flow resistance, mean velocity, Reynolds stress, and turbulent vortex structures, as well as the streamwise elongated streaky

structure and large-scale coherent structure by the K–H instability.

Nomenclature

C_{fp} : skin friction coefficient of a porous wall

C_{fs} : skin friction coefficient of a top solid wall

d_p : zero-plane displacement

D_1 : square hole size for a perforated plate

D_2 : pitch of square holes for a perforated plate

E_{xx} : one-dimensional streamwise spectral density

E_{zz} : one-dimensional spanwise spectral density

h : porous wall thickness

h_r : equivalent roughness height

H : channel height

K : mean permeability: $K = (K_{11} + K_{22} + K_{33})/3$

K_{ij} : permeability tensor

L_x : streamwise length of a computational domain

L_y : wall-normal length of a computational domain

L_z : spanwise length of a computational domain

ℓ_g : gap between perforated plates

ℓ_h : thickness of a perforated plate

p : pressure

R_{ij} : x-z plane averaged Reynolds stress

Re_τ : friction Reynolds number: $\mathrm{Re}_\tau = u_\tau(H-h)/(2\nu)$

Re_τ^p : friction Reynolds number for a porous wall: $\mathrm{Re}_\tau^p = u_{\tau p}\delta_p/\nu$

Re_τ^s : friction Reynolds number for a top solid wall: $\mathrm{Re}_\tau^s = u_{\tau s}\delta_s/\nu$

Re_b : bulk mean Reynolds number: $Re_b = U_b H/\nu$

Re_{bc} : bulk mean Reynolds number in the clear flow region: $Re_b = U_{bc}(H-h)/\nu$

t : time

u_i : velocity

u_τ : bulk friction velocity

$u_{\tau p}$: friction velocity at a porous wall

$u_{\tau s}$: friction velocity at a smooth wall

U_b : bulk mean velocity

U_{bc} : bulk mean velocity in the clear flow region

x : streamwise coordinate

y : wall-normal coordinate

z : spanwise coordinate

δ_p : boundary-layer thickness for a porous wall side

δ_s : boundary-layer thickness for a top solid wall side

κ_x : wavenumber for streamwise spectra

κ_z : wavenumber for spanwise spectra

λ_x : wavelength for streamwise spectra

λ_z : wavelength for spanwise spectra

$\lambda_{x,u}$: representative wavelength for streamwise spectrum of streamwise velocity fluctuations

$\lambda_{x,p}$: representative wavelength for streamwise spectrum of pressure fluctuations

$\lambda_{z,u}$: representative wavelength for spanwise spectrum of streamwise velocity fluctuations

ν : kinematic viscosity

τ_w : bulk wall shear stress

τ_{wp} : wall shear stress at a porous wall

τ_{ws} : wall shear stress at a solid wall

ρ : fluid density

φ : porosity

$\overline{\phi}$: Reynolds averaged value of variable ϕ

ϕ' : temporal fluctuation of variable ϕ : $\phi - \overline{\phi}$

$()^+$: values normalised by the bulk friction velocity

$()^{p+}$: values normalised by the friction velocity at a porous wall

$()^{s+}$: values normalised by the friction velocity at a solid wall

2. Numerical method

Owing to the simplicity of the wall treatment and the high spatial locality of the calculations, the lattice Boltzmann method (LBM) was used to achieve considerable success in the massive parallel computing of complex flow simulations. Furthermore, its low numerical dissipation and dispersion result in success in the DNS of fundamental turbulent flows (Lammers et al., 2006; Chikatamarla et al., 2010; Bespalko et al., 2012; Suga et al., 2015).

In the case of the LBM, there are several possible choices for discrete velocity and collision models for three-dimensional simulations. In the present study, the D3Q27 multiple-relaxation-time lattice Boltzmann method (MRT-LBM) is selected, which was previously developed by our group and rigorously validated by conducting DNSs of a turbulent channel flow, a pipe flow, a duct flow, and porous medium flows (Suga et al., 2015). Furthermore, the developed scheme was successfully applied to turbulent flows in complicated geometries, such as flows in porous media (Kuwata and Suga, 2015), and flows over porous walls (Kuwata and Suga, 2016b, 2017) and rough walls (Kuwata and Kawaguchi, 2019, 2018).

The time evolution of the particle distribution function $\boldsymbol{f}$ of the MRT-LBM can be written as

$$| \boldsymbol{f}(\boldsymbol{x}+\boldsymbol{\xi}_\alpha \delta t, t+\delta t)\rangle - | \boldsymbol{f}(\boldsymbol{x},t)\rangle = - \boldsymbol{M^{-1}}\hat{\boldsymbol{S}}\left[| \boldsymbol{m}(\boldsymbol{x},t)\rangle - | \boldsymbol{m^{eq}}(\boldsymbol{x},t)\rangle\right], \tag{3}$$

where $|\boldsymbol{f}\rangle$ is $|\boldsymbol{f}\rangle = (f_0, f_1, \cdots, f_{Q-1})^T$, and δt is the time step. It should be noted that for the D3Q27 model, $Q = 27$. The discrete velocity vector components are

$$[\boldsymbol{\xi}_0\ \boldsymbol{\xi}_1\ \boldsymbol{\xi}_2\ \boldsymbol{\xi}_3\ \boldsymbol{\xi}_4\ \boldsymbol{\xi}_5\ \boldsymbol{\xi}_6\ \boldsymbol{\xi}_7\ \boldsymbol{\xi}_8\ \boldsymbol{\xi}_9\ \boldsymbol{\xi}_{10}\ \boldsymbol{\xi}_{11}\ \boldsymbol{\xi}_{12}\ \boldsymbol{\xi}_{13}\ \boldsymbol{\xi}_{14}\ \boldsymbol{\xi}_{15}\ \boldsymbol{\xi}_{16}\ \boldsymbol{\xi}_{17}\ \boldsymbol{\xi}_{18}\ \boldsymbol{\xi}_{19}\ \boldsymbol{\xi}_{20}\ \boldsymbol{\xi}_{21}\ \boldsymbol{\xi}_{22}\ \boldsymbol{\xi}_{23}\ \boldsymbol{\xi}_{24}\ \boldsymbol{\xi}_{25}\ \boldsymbol{\xi}_{26}]/c$$

$$= \begin{bmatrix} 0 & 1 & 0 & -1 & 0 & 0 & 0 & 1 & -1 & -1 & 1 & 1 & 0 & -1 & 0 & 1 & 0 & -1 & 0 & 1 & -1 & -1 & 1 & 1 & -1 & -1 & 1 \\ 0 & 0 & 1 & 0 & -1 & 0 & 0 & 1 & 1 & -1 & -1 & 0 & 1 & 0 & -1 & 0 & 1 & 0 & -1 & 1 & 1 & -1 & -1 & 1 & 1 & -1 & -1 \\ 0 & 0 & 0 & 0 & 0 & 1 & -1 & 0 & 0 & 0 & 0 & 1 & 1 & 1 & 1 & -1 & -1 & -1 & -1 & 1 & 1 & 1 & 1 & -1 & -1 & -1 & -1 \end{bmatrix}, \tag{6}$$

where $c = \Delta/\delta t$ with Δ is the lattice spacing. The matrix $\boldsymbol{M}$ is a $Q \times Q$ matrix that linearly transforms the distribution functions to the moments as $|\boldsymbol{m}\rangle = \boldsymbol{M}|\boldsymbol{f}\rangle$. The equilibrium moment $\boldsymbol{m^{eq}}$ is obtained as $|\boldsymbol{m^{eq}}\rangle = \boldsymbol{M}|\boldsymbol{f^{eq}}\rangle$ with

$$f_\alpha^{eq} = w_\alpha \left(\rho + \rho_0 \left[\frac{\boldsymbol{\xi}_\alpha \cdot \boldsymbol{u}}{c_s^2} + \frac{(\boldsymbol{\xi}_\alpha \cdot \boldsymbol{u})^2 - c_s^2|\boldsymbol{u}|^2}{2c_s^4}\right]\right), \tag{4}$$

where $\boldsymbol{u}$ is the fluid velocity, and ρ is expressed as the sum of the constant and fluctuation values: $\rho = \rho_0 + \delta\rho$ (He and Luo, 1997). The normalised sound speed is $c_s/c = 1/\sqrt{3}$ and w_α is the weighted coefficient. The collision matrix $\hat{\boldsymbol{S}}$ is diagonal:

$$\hat{\boldsymbol{S}} \equiv diag(0, 0, 0, 0, s_4, s_5, s_5, s_7, s_7, s_7, s_{10}, s_{10}, s_{10}, s_{13}, s_{13}, s_{13}, s_{16}, s_{17}, s_{18}, s_{18}, s_{20}, s_{20}, s_{20}, s_{23}, s_{23}, s_{23}, s_{26}). \tag{5}$$

The set of relaxation parameters used in this study is as follows.

$$s_4 = 1.54, \quad s_5 = s_7, \quad s_{10} = 1.5, \quad s_{13} = 1.83, \quad s_{16} = 1.4,$$
$$s_{17} = 1.61, \quad s_{18} = s_{20} = 1.98, \quad s_{23} = s_{26} = 1.74. \tag{6}$$

The relaxation parameters s_5 and s_7 are related to the kinematic viscosity ν:

$$\nu = c_s^2 \left(\frac{1}{s_5} - \frac{1}{2} \right) \delta t = c_s^2 \left(\frac{1}{s_7} - \frac{1}{2} \right) \delta t. \tag{7}$$

Suga et al. (2015) may be referred to for the equilibrium moments $\boldsymbol{m^{eq}}$, transformation matrix $\boldsymbol{M}$, and weighted coefficients w_α.

3. Turbulent flow in a channel with a porous wall

We perform a DNS of a fully developed turbulent flow in a channel with a permeable porous wall, as illustrated in Fig.1. A computational domain size of $L_x \times L_y \times L_z$ is $6H(x) \times H(y) \times 3H(z)$, and a porous medium comprising perforated plates is considered in the lower side of the channel region $0 < y < h$ with $h/H = 0.375$. Periodic boundary conditions are applied to the streamwise and spanwise boundary faces, and no-slip walls are considered at the walls at $y = 0$ and $y = H$. The Reynolds number based on the bulk mean velocity U_b and channel height H is fixed at $\mathrm{Re}_b = 3000$, where the bulk mean velocity is defined based on the mean flow rate Q of the entire domain (porous and clear fluid regions), and the channel height H is defined as $U_b = Q/H$. A streamwise pressure difference is maintained at a constant value and adjusted in order to yield the desired flow rate. Simulations are run for a 200 large-eddy turnover time, where the large-eddy turnover time is defined as L_x/U_b.

3.1. Definition of the wall shear stress

In the present flow system, the wall shear stress at the top solid wall $\tau_{ws} = \rho(u_{\tau s})^2$ is directly computed, whereas the averaged wall shear stress at the porous wall τ_{wp} is estimated based on a balance between the bulk wall shear stress $\tau_w = (\tau_{wp} + \tau_{ws})/2$ and pressure drop ΔP in the clear channel region as follows:

$$2\tau_w L_x L_z = (H - h) L_z \Delta P. \tag{8}$$

where h denotes the porous wall thickness; thus $H - h$ stands for the clear channel height. Thus, the bulk friction velocity $u_\tau = \sqrt{\tau_w/\rho}$ and the porous wall friction velocity $u_{\tau p} = \sqrt{\tau_{wp}/\rho}$ are respectively derived as follows:

$$u_\tau = \sqrt{0.5 \frac{H-h}{L_x} \frac{\Delta P}{\rho}}, \quad u_{\tau p} = \sqrt{\frac{H-h}{L_x} \frac{\Delta P}{\rho} - \frac{\tau_{ws}}{\rho}}. \tag{9}$$

In the following discussion, the values with the superscript "$+$ ", "$p+$ " , and "$s+$ " represent the values normalised by the bulk friction velocity u_τ, friction velocity at the porous wall $u_{\tau p}$, and that at the smooth top wall $u_{\tau s}$, respectively.

3.2. Porous media and simulation parameters

In a perforated plate that consists the present porous media, square holes of D_1 with a pitch of D_2 are created in a staggered arrangement, as illustrated in Fig.1 (b). The thickness of the plate is $\ell_p = 7.8 \times 10^{-3} H$, and the plates are piled up with a horizontal offset $D_2/2$ in the $x-$ and $z-$directions with a constant vertical gap $\ell_g = 8.6 \times 10^{-2} H$, as illustrated in Fig.1(c). Furthermore, a ligament is maintained constant as $D_1 - D_2 = 7.8 \times 10^{-3} H$. This configuration enables us to extensively vary the wall permeability of

the porous media while maintaining the porous medium height at a constant value. We have to emphasize here that the goal of this study is to elucidate the influence of wall-permeability on turbulence but not to reproduce a turbulent flow over realistic perforated plates. Indeed, the perforated plates under consideration levitate unphysically; still, the main findings obtained in this study remain valid. The porous medium characteristics, including the square hole size D_1, pitch D_2, porosity φ, and permeability tensor K_{ii} are listed in Table 1. To obtain the permeability tensor via Eq.(1), the present study performs preliminary simulations of fully developed porous medium flows at a sufficiently low Reynolds number. The streamwise (spanwise) and wall-normal components are given by the pressure drop ΔP and Darcian velocity U_i obtained from simulations with the pressure difference in parallel and perpendicular directions of the plate, respectively. The Reynolds number is set to be sufficiently low ($D_1 U_i/\nu << 1.0$) to simulate flows in the Darcy regime in which ΔP is proportional to U_i, as expressed in Eq.(1). The flow characteristics: the bulk mean Reynolds number in the clear flow region Re_{bc}, bulk friction Reynolds number $\mathrm{Re}_\tau = u_\tau(H-h)/(2\nu)$, friction Reynolds number at the porous wall $\mathrm{Re}_\tau^p = u_{\tau p}\delta_p/\nu$, that at the smooth wall $\mathrm{Re}_\tau^s = u_{\tau s}\delta_s/\nu$, the mean permeability Reynolds number $\mathrm{Re}_K = \sqrt{K}u_\tau/\nu$, and the boundary layer thickness for the porous medium side $\delta_p/(H-h)$ and that for the solid wall side $\delta_s/(H-h)$ are listed in Table 2. For comparison, the DNS results of a turbulent channel flow at $\mathrm{Re}_b = 3200$ from Iwamoto et al. (2002) are also included in Table 2. Here, K is the mean permeability that is defined as the arithmetic mean value $K = (K_{11} + K_{22} + K_{33})/3$ as in Suga et al. (2018); the boundary layer thickness for the porous wall side,

and the one for the solid wall side are defined as in Breugem et al. (2006):

$$\delta_p = (H-h)\frac{\tau_{wp}}{\tau_w}, \quad \delta_s = (H-h)\frac{\tau_{ws}}{\tau_w}. \tag{10}$$

The simulation case is referred to as ReK X, where X corresponds to the mean permeability Reynolds number Re_K, as shown in Table 2. The porosity of the considered porous medium is almost unchanged at $\varphi = 0.95 - 0.99$, while the streamwise permeability varies significantly from $K_{xx}/H^2 = 2.8 \times 10^{-3}$ to 77×10^{-3}. The present porous media have an anisotropic permeability tensor, and the ratio K_{xx}/K_{yy} is greater than unity (ranging from $K_{xx}/K_{yy} = 24$ in the case of ReK14 to $K_{xx}/K_{yy} = 1.3$ in the case of ReK118), which indicates that the present porous medium tends to allow a fluid to flow into the streamwise direction rather than the wall-normal direction. It should be noted that the values of the off-diagonal components are zero in the present coordinate system. According to the DNS study on a turbulent channel flow over a porous wall of $\varphi = 0.95$, from Breugem et al. (2006), the influence of the porosity variation on the momentum and turbulence transports is very small at the interface region. Therefore, we can assume that the porosity of the present porous medium is sufficiently high that the influence of the porosity variation is negligible.

Table 2 confirms that, in the presently tested cases, the friction Reynolds number at the porous wall Re_τ^p is all larger than that at the top solid wall Re_τ^s, which suggests that turbulent friction drag is always increased by the porous wall. However, it is noted that the value of Re_τ in case Rek14 agrees with the value for the smooth wall case within 4%; thus, the influence of the porous wall is found to be negligibly small in case Rek14. Corresponding to the increase in the turbulent friction drag over the porous wall, the turbulent

boundary layer over the porous wall δ_p becomes thicker than that for the solid wall side δ_s; thus, the friction Reynolds number at the solid wall Re_τ^s is further decreased with an increase in Re_τ^p. The range of the simulated friction Reynolds number at the porous wall ($\mathrm{Re}_\tau^p = 106 - 345$) is comparable to those in previous porous-resolved-DNS studies (Kuwata and Suga, 2016b, 2017), whereas the present simulations involve a wider range of mean permeability Reynolds number ($\mathrm{Re}_K = 14 - 118$), which has yet to been studied numerically. Although the bulk mean Reynolds number is fixed at 3000, the bulk mean Reynolds number in the clear flow region, Re_{bc}, decreases with the permeability because the flow rate inside the porous medium increases with the permeability. Note that a relation $\mathrm{Re}_b = \mathrm{Re}_{bc}$ is satisfied only when there is no flow within the porous wall region.

We have to stress here that, in the present study, Re_K is employed as a parameter that characterises flow regimes over the porous wall; however, we should acknowledge that Re_K may not be the most suitable parameter for the flow characterisation over the present porous media. This is because Re_K cannot reflect the influence of the anisotropic permeability effects. Although the wall-permeability tensor, especially that in the streamwise component, is one of the most influential factors for turbulence modification (Suga et al., 2010; Kuwata and Suga, 2017; Suga et al., 2018), how the anisotropic permeability tensor affects turbulence still remains unknown because extensive investigations are required for elucidating the influence of all the components of the anisotropic permeability tensor. Another reason is that Re_K cannot reflect the inertial effects. The permeability can be used to measure the viscous flow resistance that dominates in low-Reynolds-number porous

medium flows, while the effects of the inertial force dominate the flow when the pore/grain-based Reynolds number is increased (Dybbs and Edwards, 1984). In addition, it should be noted that the influence of the bottom wall at $y = 0$ may not be negligible for highly permeable wall cases in which the blocking of the flow owing to the porous wall is considerably weakened; however, increasing the porous wall thickness depending on the permeability is impractical. Therefore, the influence of the anisotropic permeability, inertial effects, and porous wall thickness should be taken into consideration at least for exploring a parameter that can satisfactorily characterise the flow regime. This has not been focused on in the present investigation but will be the focus of future work.

3.3. Grid resolution and domain size

In order to resolve small-scale eddies generated around the porous wall while reducing the computational costs involved, we use the grid refinement technique. A regular grid domain of $768(x) \times 66(y) \times 385(z)$ is used for the area apart from the porous wall $0.5 < y/H < 1.0$, while a twice-refined grid domain of $1536(x) \times 130(y) \times 769(z)$ is allocated immediately around the porous wall $0 < y/H < 0.5$. At an interface region between the fine and coarse grid domains, we use an imbalance correction zonal grid refinement method Kuwata and Suga (2016a), which strictly guarantees the mass and momentum conservations at the grid interfaces. In the present simulation, we apply the half-way bounce-back scheme, which prescribes no-slip conditions at the wall located between the fluid and solid nodes for second-order accuracy. Hence, the uniform grid is arranged such that the surfaces of the perforated plates and walls are located at the middle between the fluid and

solid nodes. The grid resolution is confirmed to be sufficiently fine to obtain a grid-independent solution by comparing the turbulence intensity with that obtained in the simulation with a 1.5-times finer mesh in each direction for case ReK48 in which the resolution normalised by the porous wall unit is the coarsest (2.2 wall units) in the tested cases. The difference in the turbulence intensity is confirmed to be less than 0.8% at most. In addition, the computational domain size is also validated by comparing the simulation results with those obtained in larger box simulations. It is well known that large-scale perturbations originating from the K–H instability are induced over a porous wall. Kuwata and Suga (2017); Suga et al. (2018) reported that the streamwise wavelength normalised by the boundary layer thickness was approximately $3-5$, which can be adequately captured by the presently used box because $L_x/\delta_p = 6.2 - 9.2$. Furthermore, it should be noted that the present simulation box is comparable to those employed in the other DNS studies for porous-walled turbulent channel flows (iménez et al., 2001; Breugem et al., 2006; Kuwata and Suga, 2017; Rosti et al., 2015).

4. Results and Discussion

4.1. Skin friction coefficient and mean velocity

The skin friction coefficients at the porous wall, $C_{fp} = \tau_{wp}/(0.5U_b^2)$, and that at the top smooth wall, $C_{fs} = \tau_{ws}/(0.5U_b^2)$, are plotted against the mean permeability Reynolds number Re_K in Fig. 2. The skin friction coefficient at the porous wall C_{fp} is substantially larger than C_{fs} in all the cases. The increase in C_{fp} is marginal at $\mathrm{Re}_K = 14$, whereas C_{fp} increases drastically with Re_K in the range of $\mathrm{Re}_K = 14 - 48$, and it then gradually

decreases with Re_K. The increase in C_{fp} can be attributed to an increased momentum exchange due to the enhanced turbulence over the porous wall, as reported in the literature (e.g., Zagni and Smith, 1976; Zippe and Graf, 1983; Suga et al., 2010). It is interesting to note that the skin friction coefficient at the top smooth wall C_{fs} changes slightly corresponding to the change in C_{fp}. This observation implies that the influence of the porous wall may reach the other side of the top solid wall (this will be further discussed in terms of turbulence structure in §4.3). However, the increase in C_{fp} in case ReK14, in which the ratio of the streamwise permeability to the wall-normal permeability is $K_{xx}/K_{yy} = 24$, is inconsistent with recent observations in a turbulent flow over anisotropic porous media; (Rosti et al., 2018) reported through a DNS with a macroscopic porous wall model that drag reduction was achieved when the anisotropic parameter K_{xx}/K_{yy} was greater than 16. A major reason for this inconsistency can be obtained from the mean velocity U^+ profiles averaged over the fluid phase in the x–z plane, as shown in Fig. 3. Rosti et al. (2018) reported that drag reduction could be realised with an increased slippage velocity at the porous wall interface; however, we can observe from Fig. 3(a) that the slippage velocity at the porous wall interface ($y/H = 0.375$) is nearly zero in case ReK14. This difference can be attributed to the inhomogeneous nature of the presently used porous media. Rosti et al. (2018) modelled a porous medium as a homogeneous medium. In contrast, the present porous media reduce the fluid flows in the vicinity of the perforated plates but allow the fluid to flow in the middle between the plates, thus resulting in the formation of wavy profiles, as observed in Fig. 3. When we focus on the flows over the porous wall $y/H > 0.375$, the maximum

value of U^+ decreases as Re_K increases from 14 to 48 in Fig. 3 (a), and the velocity profiles tend to become skewed owing to the increase in the porous wall skin friction, as shown in Fig. 2. As Re_K further increases ($\mathrm{Re}_K > 48$) in Fig. 2 (b), the maximum value of U^+ starts to increase corresponding to the decrease in C_{fp} in Fig. 2. The decrease in C_{fp} for $\mathrm{Re}_K > 48$ can be partially explained by the U^+ profiles: the increase in Re_K also increases the slippage velocity at the porous wall interface in Fig. 2 (b), thus reducing the mean velocity gradient that contributes to turbulence generation. It is worth noting that a downward shift of inner-scale mean velocity generally represents an increase in the skin friction coefficient. However, the skin friction coefficient in case ReK37 is greater than that in case ReK48; nevertheless, the maximum value of U^+ in case ReK37 is greater than that in case ReK48. This contradiction is caused by the flow inside the porous medium: U^+ inside the porous medium region $0 < y/H < 0.375$ in case ReK48 is greater than that in case ReK37, and consequently, the flow rate across the entire domain is increased to a greater extent in case ReK48, thus resulting in a smaller skin friction coefficient.

In order to discuss the characteristics of the streamwise mean velocity profile, Fig. 5 presents the inner-scaled mean velocity profiles, following the modified log-law:

$$U^{p+} = \frac{1}{\kappa} \ln \left\{ \frac{(y' + d_p)^{p+}}{h_r^{p+}} \right\}, \tag{11}$$

where y' denotes the distance from the porous interface: $y' = y - h$, and the parameters κ, d_p, and h_r represent the Kármán constant, zero-plane displacement, and equivalent roughness height, respectively (see Breugem et al. (2006) or Suga et al. (2010) for the procedure to obtain the parameters).

For the purpose of a comparison, the smooth-wall DNS result at $\mathrm{Re}_\tau = 100$ from Iwamoto et al. (2002) is plotted. In Fig. 5(a), the profile for case ReK14 shifts slightly downward as compared with that for a smooth wall, thus suggesting a slight increase in the skin friction at the porous wall. The downward shift relative to the smooth wall result, which substantiates the increased skin friction, is increased with an Re_K value in the range of $\mathrm{Re}_K = 14-48$, as shown in Fig. 5(a), whereas it is decreased as Re_K further increases ($\mathrm{Re}_K > 48$). Corresponding to the increase in the downward shift, it is observed in the figure that the mean velocity profile also shifts rightward, owing to the increased streamwise mean flow penetration into the porous wall that is reflected by the increase in d_p^{p+}. Another observation is that the Kármán constant varies with Re_K: the slope in the logarithmic region becomes steeper as compared with that for a smooth wall when $\mathrm{Re}_K = 37 - 83$. The characteristic parameters of κ, d_p, and h_r are plotted in Fig. 4 along with the experimental data in Manes et al. (2011); Suga et al. (2010) and the DNS data in Kuwata and Suga (2016b, 2017). The Kármán constant κ is plotted against the ratio d_p/δ_p in Fig. 4(a), following Manes et al. (2011); Kuwata and Suga (2017) while Fig. 4(b) plots d_p^{p+} versus h_r^{p+}. When $\mathrm{Re}_K \leq 37$, κ in Fig. 4(a) monotonically decreases with Re_K, which supports the discussion in Manes et al. (2011) that the decrease in κ is associated with a poor separation between the inner and outer length scales, and κ can be scaled to some extent using the ratio of the boundary-layer thickness and zero-plane displacement. However, κ does not continue to decrease but its value reaches a plateau when $37 < \mathrm{Re}_K < 83$. Moreover, κ in case ReK118 is significantly larger than that in case ReK48 even though the values of

d_p/δ_p in cases ReK118 and ReK48 are nearly identical. This observation may suggest that when the zero-plane displacement is sufficiently larger than the boundary layer thickness, κ cannot be simply expressed as a function of d_p/δ_p, and other parameters may be required to scale κ.

From Fig.4(b), we confirm a general correlation between d_p^{p+} and h_r^{p+} as in the other experimental and DNS data (Suga et al., 2010; Manes et al., 2011; Kuwata and Suga, 2016b, 2017), which substantiates the fact that an increase in the skin friction at a porous wall is associated with an increased flow penetration that is reflected by d_p^{p+}. Thus, this observation also supports the findings of Suga et al. (2010); Manes et al. (2011) that increases in d_p^{p+} and h_r^{p+} could be associated with the relaxation of the wall-blocking; thus, they could be characterised by Re_K. However, when we take a close look at the present results, we observe that the values of d_p^{p+} in cases ReK37 and 118 are rather close ($d_p^{p+} = 80$ in case ReK37; $d_p^{p+} = 60$ in case ReK118) whereas the value of h_r^{p+} in case ReK37 is 4.4 times greater than that in case ReK118. This observation indicates that an increase in flow penetration does not necessary result in an increase in turbulent friction drag. It is widely accepted that turbulent velocity fluctuations produced over a porous wall penetrate the porous wall, leading to the enhancement of turbulence Pokrajac and Manes (2009); Suga et al. (2010). However, the streamwise sub-surface flow beneath the porous wall interface is also increased by the wall permeability, which is reflected by the increase in d_p^{p+} with Re_K. This in turn increases the slippage velocity at the porous interface, as shown in Fig.3, thus resulting in a reduction in the mean velocity gradient and a decreasing in the turbulent friction drag. It can be deduced from these

observations that the proposed relations among d_p, h_r, and κ may not work well for a turbulent flow over an excessively highly permeable wall, and some modifications are required to improve the correlation functions. However, as the present tested porous media are limited, it is unfortunately impossible to explore the universal correlation functions among κ, d_p, and h_r. Further investigations, especially for highly permeable porous walls, are required.

4.2. Reynolds stress

To better understand turbulence, Fig. 6 presents the profiles of the streamwise and wall-normal Reynolds stresses R_{ij}. The Reynolds stresses R_{ij} are averaged over the fluid phase in the x–z plane and normalised by the bulk friction velocity. In Fig. 6(a) and (c), the profiles of the streamwise component R_{11} and wall-normal component R_{22} are almost symmetrical in case ReK14 because the porous wall in case ReK14 behaves almost like a solid wall, which is consistent with the observation in the mean velocity profile. In contrast, as Re_K increases, the profiles become more asymmetric. The wall-normal component R_{22} is enhanced significantly over the porous walls for $\mathrm{Re}_K > 25$ while the maximum peak value of R_{11} is reduced, which is considered to be due to the destruction of the streamwise streaks owing to the enhanced wall-normal velocity fluctuation as reported by (Breugem et al., 2006; Kuwata and Suga, 2016b) (the detailed discussions of the turbulence structure are presented in §4.3). However, the maximum peak value of R_{11} does not continue to decrease as Re_K increases, and it remains nearly unchanged over the porous walls for $\mathrm{Re}_K \geq 48$. In addition, it is observed from Fig.6(a) and (b) that the streamwise turbulence intensity $\sqrt{R_{11}}^{+}$ linearly decreases with respect to y/H in the region $0.4 < y/H < 0.7$, whereas

the streamwise component inside the porous wall continues to increase with Re_K. This suggests that the increase in the wall permeability contributes more to the turbulence generation inside the porous wall rather than that over the porous wall when $\mathrm{Re}_K \geq 48$. As shown in Fig. 6(c) and (d), R_{22} is significantly enhanced owing to the relaxation of the wall-blocking effects over the porous walls for $\mathrm{Re}_K \geq 25$, while the maximum peak value of R_{22} over the porous wall decreases slightly as Re_K increases when $\mathrm{Re}_K \geq 48$.

In addition to the intensity of the turbulent velocity fluctuations, the Reynolds stress correlation coefficient between the wall-normal and streamwise velocity fluctuations, defined as $r_{12} = -R_{12}/(\sqrt{R_{11}}\sqrt{R_{22}})$, is of great importance because it reflects the coherence of the wall-ward turbulent motion. As shown in Fig.7(a) and (b), r_{12} over the porous walls for $\mathrm{Re}_K \geq 25$ is found to be considerably greater than that in case ReK14: the maximum peak value in case ReK48 is 0.64, which is twice as large as that in case ReK14. This suggests the presence of considerably coherent wall-ward turbulence motion over the porous walls in the case of $\mathrm{Re}_K \geq 25$. The maximum peak of r_{12} over the porous wall has an almost constant value irrespective of Re_K when $25 \leq \mathrm{Re}_K \leq 48$; however, r_{12} gradually decreases as Re_K further increases ($\mathrm{Re}_K > 48$). The figure confirms that r_{12} decreases when it departs from the porous wall, while r_{12} inside the porous wall exhibits a wavy profile corresponding to the location of the perforated plates. Interestingly, the considerably enhanced r_{12} over the porous walls in cases ReK25, ReK37, and ReK48 is still retained deep inside the porous wall region. Thus, as reported by Kuwata and Suga (2016b), the increase in r_{12} over the porous walls can be attributed to the large-scale streamwise coherent perturbations originat-

ing from the K–H instability (Finnigan, 2000; iménez et al., 2001; Breugem et al., 2006; Kuwata and Suga, 2016b), and the increase in r_{12} deep inside the porous wall is driven by the large-scale perturbations that penetrate the porous wall. Indeed, Kuwata and Suga (2016b) reported that the large-scale coherent structures by the K–H instability initiated over the porous wall induced large-scale coherent structures deep inside the porous wall. It is noted here that the finding in Fig.6, i.e., that the streamwise turbulence intensity is decreased while the wall-normal turbulence intensity is increased, is in accordance with the results of turbulence over the vegetation canopy. Moreover, the maximum value of r_{12} in the case of $\mathrm{Re}_K \geq 25$ is $r_{12} = 0.5 - -0.6$, which is fairly close to the value in a turbulent flow over the vegetation canopy (Raupach et al., 1996). Raupach et al. (1996) reported that the maximum values of r_{12} measured in 12 separate experiments on vegetation canopy turbulence in a wind tunnel were around 0.5, suggesting that turbulent coherent structure over the canopy is more organized. This in turn implies that the turbulence over the porous wall in the case of $\mathrm{Re}_K \geq 25$ shares common features with turbulence over the vegetation canopy.

4.3. Turbulence structures

With respect to a turbulence structure over a permeable porous wall, it is well known that the development of streamwise elongated high- and low-speed streaks is prevented by significantly enhanced wall-normal turbulent motions, while large-scale streamwise perturbations, also known as spanwise rollers, originating from the K–H type of instability emerge over a porous wall (Breugem et al., 2006; Kuwata and Suga, 2016b). However, investigations through a DNS were limited to the flows at a relatively low permeability

Reynolds number. Accordingly, this subsection presents an extensive investigation of the wall-permeability effects on the turbulence modification over a porous wall. We first examine the streamwise velocity fluctuations over the porous walls at $y'^{p+} \simeq 10$ in Fig. 8, where y'^{p+} denotes the wall coordinate from the porous wall. In addition, in order to statistically quantify the length scales of the turbulent vortex structures, a two-point correlation function of streamwise velocity fluctuations is presented in Fig.9, which is defined as follows:

$$R_{uu,x_k}(\Delta x_k) = \frac{\overline{u'(x_k)u'(x_k+\Delta x_k)}}{\overline{u'(x_k)u'(x_k)}}, \tag{12}$$

where u' and Δx_k denote the streamwise velocity fluctuation and the separation, respectively. The separation Δx_k in the horizontal axis in Fig.9 is normalised by the porous wall units $u_{\tau p}/\nu$. We can observe from Fig. 8(a) that arrays of high- and low-speed streaks, which are similar to those observed over a smooth wall, are clearly developed over the porous wall in case ReK14. As half of the statistical spacing between two neighbouring streaks corresponds to a spanwise separation Δz at the negative local minimum point of $R_{uu,z}$ in Fig. 9(a), the statistical streak spacing in case ReK14 is estimated as approximately 100 wall units, which is in good agreement with that over a smooth wall (Kim et al., 1987). Therefore, it can be inferred that the porous wall in case ReK14 hardly modifies the turbulence structure, which is consistent with the almost symmetrical profiles of the mean velocity and Reynolds stress profiles in Figs.3 and 6. In contrast, Fig. 8(b) shows that the streamwise elongated streaks are absent in case ReK25, while the turbulent structure is instead elongated in the spanwise direction and perturbates in the streamwise direction. This large-scale structure can be detected from the

two-point correlation functions, as shown in Figs. 9(a) and (c): the significant coherence in the spanwise direction across the full box is confirmed from non-zero $R_{uu,z}$ at $\Delta z^{p+} = L_z^{p+}/2$ in Fig. 9(a), and the profile of $R_{uu,x}$ is wavy and exhibits the negative and positive local minimum/maximum values in Fig. 9(c). Similar observations for the two-point correlation functions were also made in iménez et al. (2001); Kuwata and Suga (2016b), wherein it was suggested that the wavy two-point correlation function profiles indicated the presence of streamwise perturbations induced by the K–H instability.

In Fig. 8(b)–(d), although the spanwise elongated structure owing to the K–H instability can be clearly observed in case ReK25, this structure is observed to be less obvious as Re_K increases. This can also be confirmed from the two-point correlation functions in case ReK48: $R_{uu,z}$ in Fig. 9(a) rapidly decreases to zero at $\Delta z^+ \simeq 200$, and $R_{uu,x}$ in Fig. 9(a) loses a secondary local maximum peak. Furthermore, as Re_K further increases from $\mathrm{Re}_K = 48$ to 118, it is observed from Fig. 8(d)–(f) that the quasi-streamwise elongated streaky structure emerges again; however, the high- and low-speed regions meander substantially in the spanwise direction, and the statistical spanwise spacing between the high- and low-speed regions appears to be much longer than that over a smooth wall. Indeed, although $R_{uu,z}$ in Fig. 9(b) exhibits a local minimum as in case ReK14, a spanwise separation at the local minimum point is of $250 - 350$ porous wall units, indicating that the statistical spanwise distance corresponds to $500 - 700$ porous wall units, which is approximately $5 - 6$ times longer than that over a smooth wall. Moreover, another important fact we can find from Fig. 9(b) is that as Re_K increases from 48 to 118, the depth of the local minimum point of $R_{uu,z}$ increases

while the spanwise separation at the local minimum point decreases. This suggests that the quasi-streamwise elongated streaky structure, the spanwise spacing of which is much longer than that over a smooth wall, tends to be narrower and increasingly organised as Re_K increases. The explanation for this modification of the turbulent structure is that the enhanced wall-normal turbulence motion, which interrupts the streak formation, is weakened as Re_K increases, as observed in Fig. 6. It is worth noting that the reduction in the spanwise coherence of the perturbation by the K–H instability and the emergence of the quasi-streamwise elongated streaky structure for $\mathrm{Re}_K \geq 48$ are consistent with the results in turbulent flows over a wheat canopy given in Shaw et al. (1995). The two-point spatial correlation analysis in Shaw et al. (1995) showed that the spanwise correlation function exhibited a negative local minimum point while the streamwise correlation function did not have a secondary local maximum peak associated with the streamwise perturbation. This trend is very similar to the present results for $\mathrm{Re}_K \geq 48$ in Fig. 9. Thus, it can be said that the simulated flows in this study over the highly permeable walls for $\mathrm{Re}_K > 48$ are similar to the turbulence over the vegetation canopy. Furthermore, these observations also demonstrate an analogy between a turbulent flow over a permeable wall and a mixing layer flow because the transition from the turbulent structure in the lower permeability case ($\mathrm{Re}_K = 25$) to the higher permeability cases ($\mathrm{Re}_K \geq 48$) shares common features with the growth of three-dimensional motion in the plane-mixing layer. Indeed, as the plane-mixing layer develops, the spanwise rollers arising from the K–H instability are less organized owing to the amalgamation processes between the neighbouring rollers, and then the dis-

tinctive streamwise elongated streaks are formed (Bernal and Roshko, 1986). The similarity of the turbulence structure between the turbulent flow over the permeable wall and the mixing layer flow in terms of the length scale will be discussed later.

To obtain greater insight into the effects of wall permeability on the length scales of the turbulent vortex structure discussed above, we discuss the wavenumber multiplied streamwise energy spectra for cases ReK14, ReK25, ReK38, and ReK118. These cases are selected owing to their characteristic structures: the turbulence structure in case ReK14 is very similar to that over a smooth wall, that in case ReK25 is dominated by the coherent large-scale structures induced by the K–H instability, and that in ReK118 loses the footprint of the K–H instability, but the quasi-streamwise streaky structure emerges again, and case ReK38 is selected as the case in which the turbulent frictional drag is the largest among the tested cases. As pressure fluctuations can reflect the influence of large-scale perturbations induced by the K–H instability well (Kuwata and Suga, 2016b), we first discuss the contour maps of the energy spectrum of pressure fluctuations $\kappa_x^+ E_{xx,p}^+$ normalised by the bulk friction velocity in Fig. 10. As it was reported by (Kuwata and Suga, 2017; Suga et al., 2018) that the wavelength of the large-scale perturbations can be reasonably scaled by the boundary layer thickness for a porous wall δ_p (Kuwata and Suga, 2017; Suga et al., 2018), $\kappa_x^+ E_{xx,p}^+$ is plotted against λ_x/δ_p in this study. In case ReK14, the outline of the contour map of the energy spectrum in the porous wall side ($y/H < 0.69$) is found to be similar to that in the solid wall side ($0.69 < y/H < 1.0$), while the maximum peak value of $\kappa_x^+ E_{xx,p}^+$ in the porous wall side is increased to 1.08, which is 40% larger

than that in the solid wall side. This means that the pressure fluctuations are distinctly enhanced over the porous wall. In cases ReK25, ReK38, and ReK118, we can observe from Fig. 10(b)—(d) that $\kappa_x^+ E_{xx,p}^+$ has a pointed peak around $\lambda_x/\delta_p \simeq 3-4$ over the porous wall. This wavelength is close to the previously reported wavelength of the large-scale structures induced by the K–H instability (Kuwata and Suga, 2017; Suga et al., 2018): Kuwata and Suga (2017) reported $\lambda_x/\delta_p \simeq 3.4$, and Suga et al. (2018) also derived $3.4 < \lambda_x/\delta_p < 5.5$ from their large amount of experimental data. Therefore, the pointed peak around $\lambda_x/\delta_p \simeq 3-4$ can be attributed to pressure fluctuations that originate from the K–H instability. The peak value of $\kappa_x^+ E_{xx,p}^+$ is the largest in case ReK25, where we can clearly identify the large-scale streamwise perturbations, as shown in Fig.8, and the peak value is found to decrease with Re_K. This finding suggests that the turbulence vortex structure induced by the K–H instability is more distinct for low-Re_K flows, which are rapidly attenuated as Re_K increases. Moreover, it is worth noting that the maximum turbulent friction drag is not achieved in case Rek25, as shown in Fig.2, wherein the streamwise perturbations by the K–H instability are the most organized and retain strong coherence in the spanwise direction. The maximum turbulent friction drag is, however, attained in case Rek38. This implies that the turbulent friction drag takes a maximum value after the transition of the large-scale structure by the K–H instability to a more chaotic structure. Another interesting observation is that the wavelength at the maximum peak is constant irrespective of the distance from the wall y/H. This demonstrates that the influence of the K–H instability is not confined to the area near the porous wall but extends even near the top solid wall.

This is also implied by the results of the proper orthogonal decomposition (POD) analysis in a porous walled turbulent channel flow by Kuwata and Suga (2016b), who reported that the large-scale structure visualised by the first POD modes prevailed over the entire region.

To better understand the length scales of turbulent vortex structures, Fig. 11 presents the contour maps of the streamwise energy spectra of streamwise velocity fluctuations $\kappa_x^+ E_{xx,u}^+$, normalised by the bulk friction velocity. In contras to the energy spectrum of pressure fluctuations in case ReK14, as shown in Fig. 10(a), the contour maps of $\kappa_x^+ E_{xx,u}^+$ near the porous and solid walls in case ReK14 (Fig. 11(a)) are nearly identical. The streamwise velocity spectrum in cases ReK25 and ReK37, as shown in Fig. 11 (b) and (c), respectively, has a peak around $\lambda_x/\delta_p \simeq 3-4$ near the porous wall as in the pressure spectrum. This is also an indication of the presence of the streamwise velocity perturbations owing to the K–H instability. Moreover, it is worth noting that the spectrum map near the top solid wall for cases ReK25 and ReK37 is distinctly different from that in case ReK14, and the spectrum near the solid wall in cases ReK25 and ReK37 has a peek around $\lambda_x/\delta_p \simeq 3-4$. Thus, this clearly indicates that the influence of the K–H instability initiating over the porous wall extends to the top solid wall, and it can be concluded that the presence of a porous wall potentially alters the turbulence even outside the boundary layer over the porous wall. Fig.11(d) shows that, in contrast to the results obtained in cases ReK25 and ReK37, the wavelength at the maximum peak of the velocity spectrum in case ReK118 ($\lambda_x/\delta_p \simeq 7$) deviates significantly from that of the pressure spectrum ($\lambda_x/\delta_p \simeq 3-4$). This means that the streamwise mean velocity fluctuations in case Rek118 are

less modulated by the pressure fluctuations. The enhancement of the velocity spectrum in the long wavelength region in case Rek118 is consistent with the observation in Fig.8 (g): the high- and low-speed regions of the streamwise velocity fluctuations tend to be elongated in the streamwise direction.

As the spanwise coherence varies significantly depending on Re_K, as observed in Fig. 8, we discuss the spanwise length scales of streamwise velocity fluctuations by analysing the spanwise spectrum of streamwise velocity fluctuations $\kappa_z^+ E_{zz,u}^+$ in Fig. 12. The wavelength in the horizontal axis is normalised by the bulk friction velocity and kinematic viscosity. The spectrum $\kappa_z^+ E_{zz,u}^+$ is plotted here against κ_z^+. The spanwise spectrum in case ReK14 has peaks around $\lambda_z^+ \simeq 100 - 200$ near the porous and solid walls, whereas the wavelength at the maximum peak over the porous wall in cases ReK25, ReK38, and ReK118 is apparently longer than that near the top solid wall. We can observe from Fig. 12(a) and (b) that $\kappa_z^+ E_{zz,u}^+$ in the vicinity of the porous wall for case ReK25 increases in strength in the long-wavelength region ($\lambda_z^+ > 1000$) as compared with that for case ReK14, which is considered to be due to the spanwise elongated structures as observed in Fig. 8. As Re_K increases, the energy spectrum in the long-wavelength region $\lambda_z^+ > 1000$ decays steeply; thus, the maximum peak around $\lambda_z^+ \simeq 800$ becomes distinct in case ReK118.

Finally, we focus on the representative wavelength of pressure and velocity fluctuations, which is defined as the wavelength that takes the maximum peak of the energy spectrum. Figure 13(a) shows the representative wavelengths of pressure fluctuations $\lambda_{x,p}$ and that of streamwise velocity fluctuations $\lambda_{x,u}$ near the porous wall, both of which are normalised by the boundary layer

thickness over the porous wall δ_p. It should be noted that as $\kappa_x^+ E_{xx,u}^+$ does not have a peak in case ReK14, the plot of $\lambda_{x,u}$ in case ReK14 is not included in the figure. We can find from the figure that $\lambda_{x,u} \simeq \lambda_{x,p}$ in cases ReK25 and ReK37, whereas $\lambda_{x,u}$ increases and deviates from $\lambda_{x,p}$ when $\mathrm{Re}_K \geq 48$. In the regime $\mathrm{Re}_K \geq 48$, the representative wavelength of the pressure fluctuations exhibits a lower value of $\lambda_{x,p}/\delta_p \simeq 2-3$ than the previous reported value for the K–H instability wave. The deviation of $\lambda_{x,u}$ from $\lambda_{x,p}$ can be attributed to the weakened pressure fluctuations associated with the K–H instability, as shown in Fig.10, that is to say, as the streamwise pressure perturbations owing to the K–H instability are too weak to break streamwise elongated structures, the streamwise elongated structures can develop over the porous wall.

The spanwise representative wavelengths of streamwise velocity fluctuations near the porous and solid walls normalised by their wall units, $\lambda_{z,u}^{p+}$ and $\lambda_{z,u}^{s+}$, are displayed in Fig 13(b): $\lambda_{z,u}$ over the porous wall is normalised by the friction velocity at the porous wall while that for the solid wall side is normalised by the friction velocity at the top solid wall. The spanwise representative wavelength near the solid wall is $\lambda_{z,u}^{s+} \simeq 100$ irrespective of Re_K. This indicates that the statistical spacing between two neighbouring streaks is consistent while, as discussed above in Fig. 11(d), the streamwise elongation is slightly suppressed by the streamwise pressure perturbations. The spanwise representative wavelength over the porous wall in case ReK14 is almost the same as that near the solid wall, while $\lambda_{z,u}^{p+}$ for $\mathrm{Re}_K \geq 25$ is significantly larger than that near the solid wall. The value of $\lambda_{z,u}^{p+}$ is approximately $400-600$ porous wall units. The ratio $\lambda_{z,u}/\lambda_{x,p}$, which represents

the ratio of the statistical spanwise spacing of the streaky structure to the characteristic wavelength of the K–H instability mode, is around $0.4 - 1.2$. This value is comparable to the experimental data in a plane-mixing layer flow given in Bernal and Roshko (1986), who reported that the ratio between the spacing of the streaks and the spacing of the spanwise roller in the plane mixing layer was around $0.5 - 0.9$. This agreement implies that the origin of the streaky structure at higher permeability Reynolds number is the same as the streaky structure in the plane-mixing layer. It also further supports the analogy between a turbulent flow over a permeable porous wall and a plane mixing layer flow.

Therefore, it can be summarised that there are two characteristic perturbation modes: the one is the streamwise perturbation mode around $\lambda_x/\delta_p \simeq 3 - 4$ induced by the K–H instability, and the other is the spanwise perturbation mode forming the streamwise streaky structure around $\lambda_z^{p+} = 400 - 600$. In cases ReK25 and ReK37, the streamwise perturbation mode overwhelms the spanwise perturbation mode; thus, the large-scale streamwise perturbation distinctly appears as observed in Fig.8. In contrast, as the streamwise perturbations owing to the K–H instability decrease in strength when $\mathrm{Re}_K \geq 37$, the turbulence structure is observed to be elongated in the streamwise direction as observed in Fig. 8. The change in the turbulent structure with the wall permeability is analogous to the transition from a two-dimensional mixing layer to a fully turbulent mixing layer. In this transition of the mixing layer, the spanwise-organized rollers primary arising from the K–H instability become less organized with the growth of the three-dimensional disturbance, and the streamwise streaks are formed Brown and

Roshko (1974); Bernal and Roshko (1986).

5. Conclusions

The influence of wall permeability on turbulence is extensively investigated by means of lattice Boltzmann direct numerical simulations of turbulent porous-walled channel flows. The bulk mean Reynolds number is fixed at 3000, and porous media consisting of perforated plates are considered in the lower side of the channel. The mean permeability Reynolds number is varied from $14 - 118$ by varying the hole size of the perforated plates. The spectral analysis reveals the presence of two characteristic perturbation modes, namely, the streamwise perturbation mode induced by the K–H instability and the spanwise perturbation mode. The streamwise perturbation mode induces the spanwise-coherent streamwise perturbation while the quasi-streamwise elongated streaky structure is developed by the spanwise perturbation mode. The wavelength of the streamwise perturbation mode is approximately three to four times as large as the boundary-layer thickness while the spanwise perturbation mode features approximately $400 - -600$ porous wall units. The ratio of the wavelength of the spanwise perturbation mode to the streamwise one is found to be comparable to that in a plane-mixing layer, suggesting the similarity between a turbulent flow over a permeable porous wall and a mixing layer flow. In the case of the lowest permeability Reynolds number, the porous wall has a slightly increased skin friction coefficient. When the mean permeability Reynolds number increases, the streamwise perturbations by the K–H instability overwhelm the spanwise perturbation mode, and the streamwise perturbations appear distinctly. As

this structure increases the coherence of the wall-ward turbulence motion, the turbulence is significantly enhanced. In this regime, the wall-normal turbulence intensity is particularly enhanced due to the relaxation of the wall-blocking effects, and a maximum increase in drag is attained. However, as the mean permeability Reynolds number increases further, the streamwise perturbation mode is rapidly reduced and the spanwise model is dominant; thus, the quasi-streamwise elongated streaky structure, the mean spacing of which is much longer than that over a smooth wall, is developed. In this regime, the turbulence enhancement is reduced because of an increased slippage velocity at the porous interface.

Acknowledgements

The authors express their gratitude to their colleague: Dr. M. Kaneda for his support. A part of this study was financially supported by the research grant (No.17K14591) of the JSPS Japan.

References

Bernal, L., Roshko, A., 1986. Streamwise vortex structure in plane mixing layers. J. Fluid Mech. 170, 499–525.

Bespalko, D., Pollard, A., Uddin, M., 2012. Analysis of the pressure fluctuations from an LBM simulation of turbulent channel flow. Comput. Fluids 54, 143–146.

Breugem, W.P., Boersma, B.J., Uittenbogaard, R.E., 2006. The influence of wall permeability on turbulent channel flow. J. Fluid Mech. 562, 35–72.

Brown, G.L., Roshko, A., 1974. On density effects and large structure in turbulent mixing layers. J. Fluid Mech. 64, 775–816.

Chikatamarla, S., Frouzakis, C., Karlin, I., Tomboulides, A., Boulouchos, K., 2010. Lattice Boltzmann method for direct numerical simulation of turbulent flows. J. Fluid Mech. 656, 298–308.

Darcy, H., 1856. Les fontaines publiques de la ville de dijon. Dalmont, Paris 647.

Dybbs, A., Edwards, R.V., 1984. A new look at porous media fluid mechanics-Darcy to turbulent, in: Bear, J., Corapcioglu, M.Y. (Eds.), Fundamentals of Transport Phenomena in Porous Media. Springer Netherlands. volume 82 of *NATO ASI Series*, pp. 199–256.

Finnigan, J., 2000. Turbulence in plant canopies. Ann. Rev. Fluid Mech. 32, 519–571.

Ghisalberti, M., Nepf, H.M., 2002. Mixing layers and coherent structures in vegetated aquatic flows. J. Geophys. Res.-Oceans 107, 3–1.

He, X., Luo, L.S., 1997. Lattice Boltzmann model for the incompressible Navier-Stokes equation. J. Stat. Phys. 88, 927–944.

Ho, R.T., Gelhar, L.W., 1973. Turbulent flow with wavy permeable boundaries. J. Fluid Mech. 58, 403–414.

iménez, J., Uhlmann, M., Pinelli, A., Kawahara, G., 2001. Turbulent shear flow over active and passive porous surfaces. J. Fluid Mech. 442, 89–117.

Iwamoto, K., Suzuki, Y., Kasagi, N., 2002. Database of fully developed channel flow-thtlab internal report no. ILR-0201, Rapport technique, THT-LAB, Dept. of Mech. Engng., The Univ. of Tokyo .

Jiménez, J., 1983. A spanwise structure in the plane shear layer. J. Fluid Mech. 132, 319–336.

Kim, J., Moin, P., Moser, R., 1987. Turbulence statistics in fully developed channel flow at low Reynolds number. J. Fluid Mech. 177, 133–166.

Kong, F.Y., Schetz, J.A., 1982. Turbulent boundary layer over porous surfaces with different surface geometries. Technical Report 82-0030. AIAA.

Kuwata, Y., Kawaguchi, Y., 2018. Direct numerical simulation of turbulence over systematically varied irregular rough surfaces. J. Fluid Mech. 862, pp.781–815.

Kuwata, Y., Kawaguchi, Y., 2019. Direct numerical simulation of turbulence over resolved and modeled rough walls with irregularly distributed roughness. Int. J. Heat Fluid Flow. 77, 1–18.

Kuwata, Y., Suga, K., 2015. Large eddy simulations of pore-scale turbulent flows in porous media by the lattice Boltzmann method. Int. J. Heat Fluid Flow 55, 143–157.

Kuwata, Y., Suga, K., 2016a. Imbalance-correction grid-refinement method for lattice Boltzmann flow simulations. J. Comput. Phys. 311, 348–362.

Kuwata, Y., Suga, K., 2016b. Lattice boltzmann direct numerical simulation

of interface turbulence over porous and rough walls. Int. J. Heat Fluid Flow 61, 145–157.

Kuwata, Y., Suga, K., 2016c. Transport mechanism of interface turbulence over porous and rough walls. Flow, Turb. Combust. 97, 1071–1093.

Kuwata, Y., Suga, K., 2017. Direct numerical simulation of turbulence over anisotropic porous media. J. Fluid Mech. 831, 41–71.

Lammers, P., Beronov, K.N., Volkert, R., Brenner, G., Durst, F., 2006. Lattice BGK direct numerical simulation of fully developed turbulence in incompressible plane channel flow. Comput. Fluids 35, 1137–1153.

Lovera, F., Kennedy, J.F., 1969. Friction factors for flat bed flows in sand channels. J. Hydr. Div., ASCE 95, 1227–1234.

Manes, C., Poggi, D., Ridol, L., 2011. Turbulent boundary layers over permeable walls: scaling and near-wall structure. J. Fluid Mech. 687, 141–170.

Manes, C., Pokrajac, D., McEwan, I., Nikora, V., 2009. Turbulence structure of open channel flows over permeable and impermeable beds: A comparative study. Phys. Fluids 21, 125109.

Nepf, H., Ghisalberti, M., 2008. Flow and transport in channels with submerged vegetation. Acta Geophysica 56, 753–777.

Pokrajac, D., Manes, C., 2009. Velocity measurements of a free-surface turbulent flow penetrating a porous medium composed of uniform-size spheres. Transp. Porous Med. 78, 367–383.

Raupach, M.R., Finnigan, J.J., Brunet, Y., 1996. Coherent eddies and turbulence in vegetation canopies: the mixing-layer analogy, in: Boundary-Layer Meteorol.. Springer, pp. 351–382.

Rosti, M.E., Brandt, L., Pinelli, A., 2018. Turbulent channel flow over an anisotropic porous wall–drag increase and reduction. J. Fluid Mech. 842, 381–394.

Rosti, M.E., Cortelezzi, L., Quadrio, M., 2015. Direct numerical simulation of turbulent channel flow over porous walls. J. Fluid Mech. 784, 396–442.

Ruff, J.F., Gelhar, L.W., 1972. Turbulent shear flow in porous boundary. J. Eng. Mech. Div., ASCE 98, 975–991.

Shaw, R., Brunet, Y., Finnigan, J., Raupach, M., 1995. A wind tunnel study of air flow in waving wheat: two-point velocity statistics. Boundary Layer Meteorol. 76, 349–376.

Suga, K., Kuwata, Y., Takashima, K., Chikasue, R., 2015. A D3Q27 multiple-relaxation-time lattice Boltzmann method for turbulent flows. Comput. Math. Appl. 69, 518–529.

Suga, K., Matsumura, Y., Ashitaka, Y., Tominaga, S., Kaneda, M., 2010. Effects of wall permeability on turbulence. Int. J. Heat Fluid Flow 31, 974–984.

Suga, K., Okazaki, Y., HO, U., Kuwata, Y., 2018. Anisotropic wall permeability effects on turbulent channel flows. J. Fluid Mech. 855, 983–1016.

White, B.L., Nepf, H.M., 2007. Shear instability and coherent structures in shallow flow adjacent to a porous layer. J. Fluid Mech. 593, 1–32.

Zagni, A.F.E., Smith, K.V.H., 1976. Channel flow over permeable beds of graded spheres. J. Hydraul. Div. 102, 207–222.

Zippe, H.J., Graf, W.H., 1983. Turbulent boundary-layer flow over permeable and non-permeable rough surfaces. J. Hydraul. Res. 21, 51–65.

Table 1: Characteristic parameters for the porous media.

Case	D_1/H	$D_1/D_2 - 1$	φ	K_{xx}/H^2, K_{zz}/H^2	K_{xx}/K_{yy}
ReK14	0.012	0.33	0.953	2.8×10^{-3}	24
ReK25	0.023	0.20	0.972	3.0×10^{-3}	12
ReK37	0.039	0.091	0.985	3.6×10^{-3}	4.0
ReK48	0.086	0.043	0.993	5.5×10^{-3}	2.0
ReK64	0.18	0.021	0.996	11×10^{-3}	1.7
ReK83	0.37	0.011	0.998	25×10^{-3}	1.6
ReK118	0.74	0.0052	0.999	77×10^{-3}	1.3

Table 2: Flow characteristics of the simulations. The bulk mean Reynolds number in the clear flow region $\mathrm{Re}_{bc} = U_{bc}(H-h)/\nu$, the bulk friction Reynolds number $\mathrm{Re}_\tau = u_\tau(H-h)/(2\nu)$, friction Reynolds number at a porous wall $\mathrm{Re}^p_\tau = u_{\tau p}\delta_p/\nu$, that at a smooth wall $\mathrm{Re}^s_\tau = u_{\tau s}\delta_s/\nu$, the mean permeability Reynolds number $\mathrm{Re}_K = \sqrt{K}u_\tau/\nu$, the boundary thickness over the porous wall $\delta_p/(H-h)$, and that for the solid wall side $\delta_s/(H-h)$. The DNS data of a turbulent channel flow at $\mathrm{Re}_b = 3200$ from Iwamoto et al. (2002) are included for reference.

Case	Re_{bc}	Re_τ	Re^p_τ	Re^s_τ	Re_K	$\delta_p/(H-h)$	$\delta_s/(H-h)$
smooth	3200	109	–	109	0.0	–	0.50
ReK14	2850	99	106	92	14	0.52	0.48
ReK25	2800	146	248	61	25	0.72	0.28
ReK37	2800	180	340	56	37	0.77	0.23
ReK48	2700	178	345	50	48	0.78	0.22
ReK64	2500	164	310	50	64	0.77	0.23
ReK83	2400	144	259	51	83	0.75	0.25
ReK118	2250	118	193	54	118	0.70	0.30

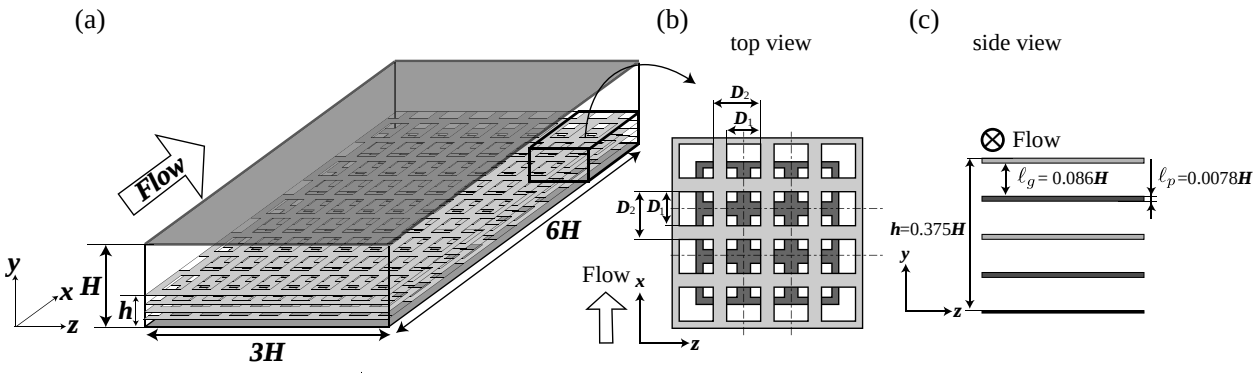

Figure 1: (a) Computational geometry of the channel with porous media, (b) top view of the porous medium, and (c) side view of the porous medium.

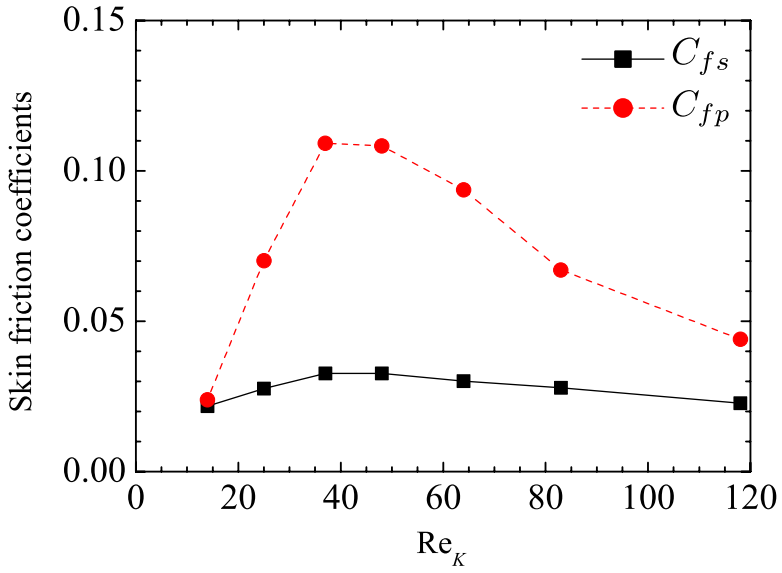

Figure 2: Variation of the skin friction coefficient of the porous wall $C_{fp} = \tau_{wp}/(\rho U_b^2)$ and that of the top smooth wall $C_{fs} = \tau_{ws}/(\rho U_b^2)$ against Re_K.

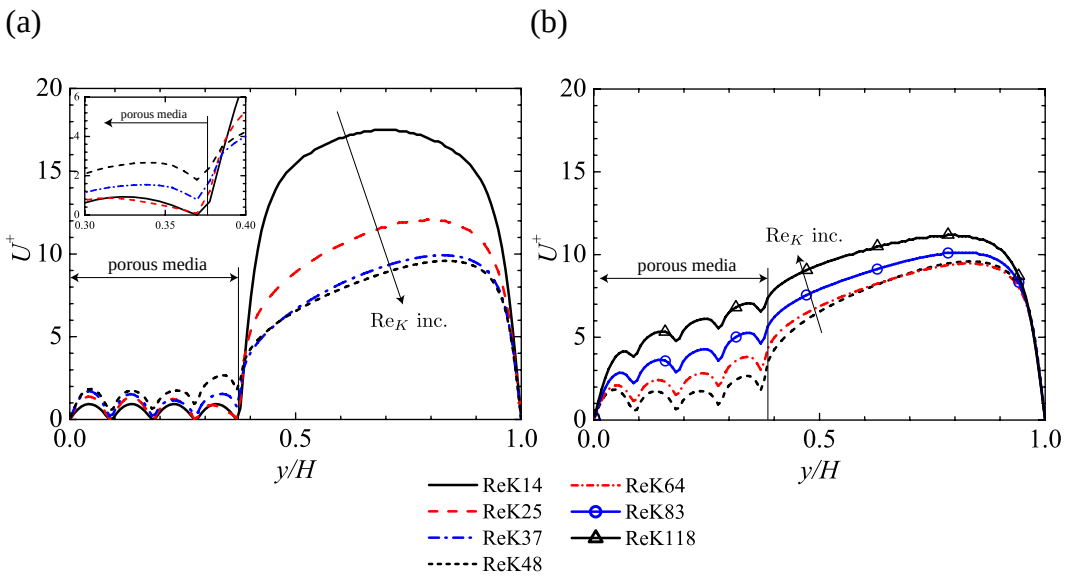

Figure 3: x–z plane-averaged streamwise mean velocity normalised by the bulk friction velocity: (a) profiles for $14 \leq \mathrm{Re}_K \leq 48$, and (b) profiles for $48 \leq \mathrm{Re}_K \leq 116$.

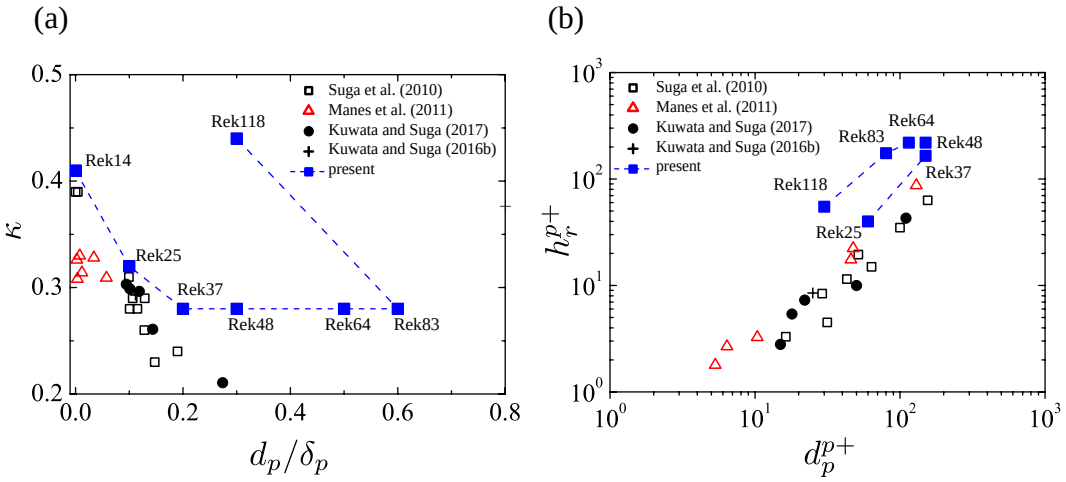

Figure 4: Characteristic parameters for the modified log-law: the Kármán constant κ, zero-plane displacement d_p, and equivalent roughness height h_r: (a) κ against d_p/δ_p, and (b) $d_p{}^p+$ against h_r^{p+}, the experimental data from Suga et al. (2010); Manes et al. (2011) and the DNS data from Kuwata and Suga (2016b, 2017) are included.

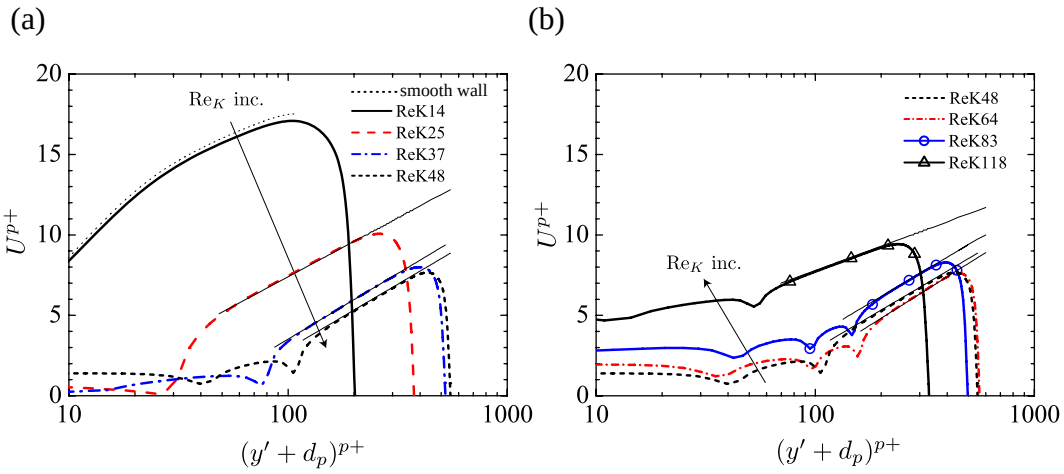

Figure 5: Modified log-law profiles: (a) profiles for $14 \leq \mathrm{Re}_K \leq 48$, and (b) profiles for $48 \leq \mathrm{Re}_K \leq 116$.

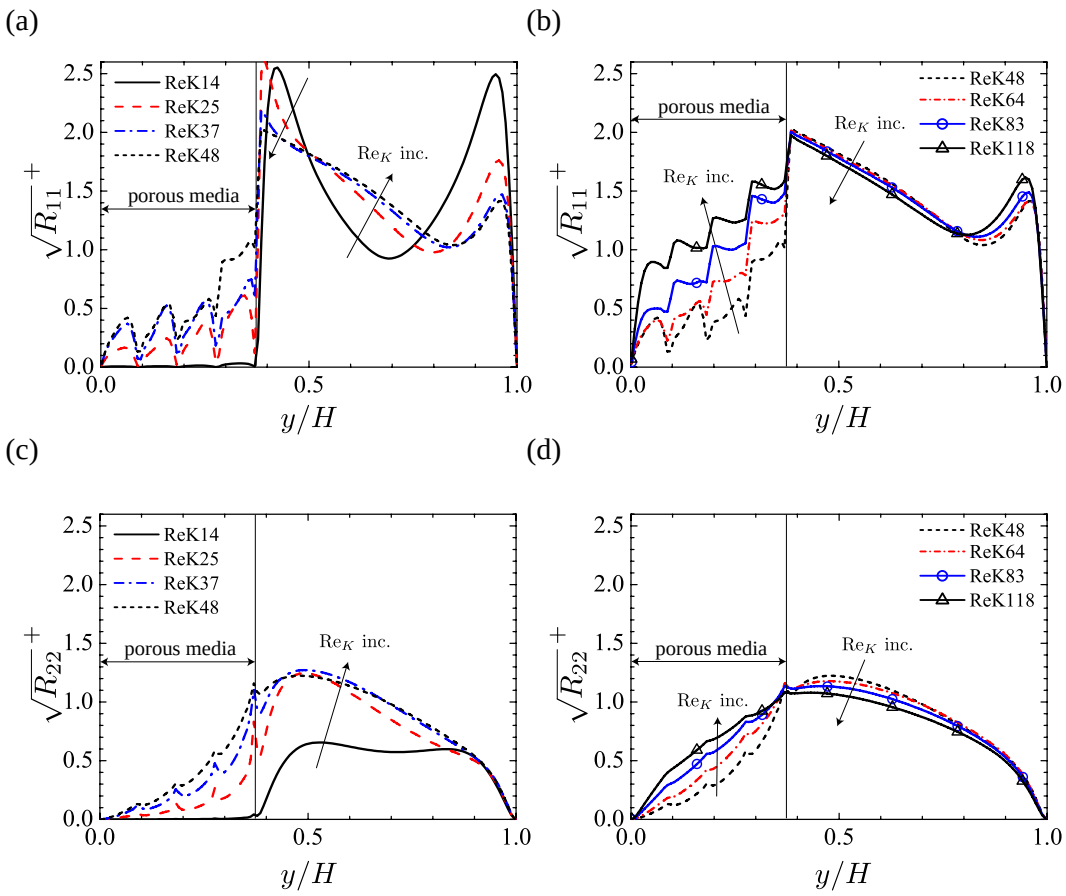

Figure 6: x–z plane-averaged Reynolds stresses of the streamwise component R_{11} and the wall-normal component R_{22}, normalised by the bulk friction velocity: (a) profiles of R_{11} for $14 \leq \mathrm{Re}_K \leq 48$, (b) profiles of R_{11} for $48 \leq \mathrm{Re}_K \leq 116$, (c) profiles of R_{22} for $14 \leq \mathrm{Re}_K \leq 48$, and (d) profiles of R_{22} for $48 \leq \mathrm{Re}_K \leq 116$.

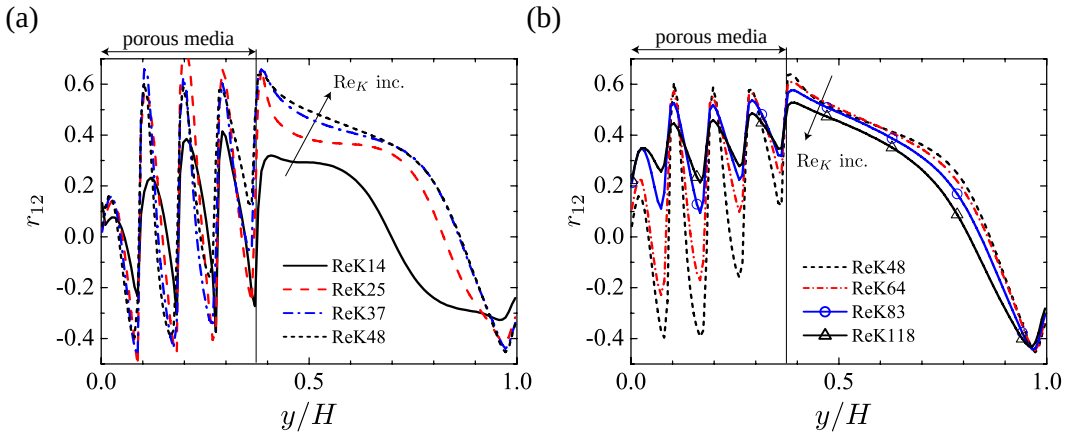

Figure 7: x–z plane-averaged Reynolds shear stress correlation coefficient r_{12}: (a) profiles for $14 \leq \mathrm{Re}_K \leq 48$, and (b) profiles for $48 \leq \mathrm{Re}_K \leq 116$.

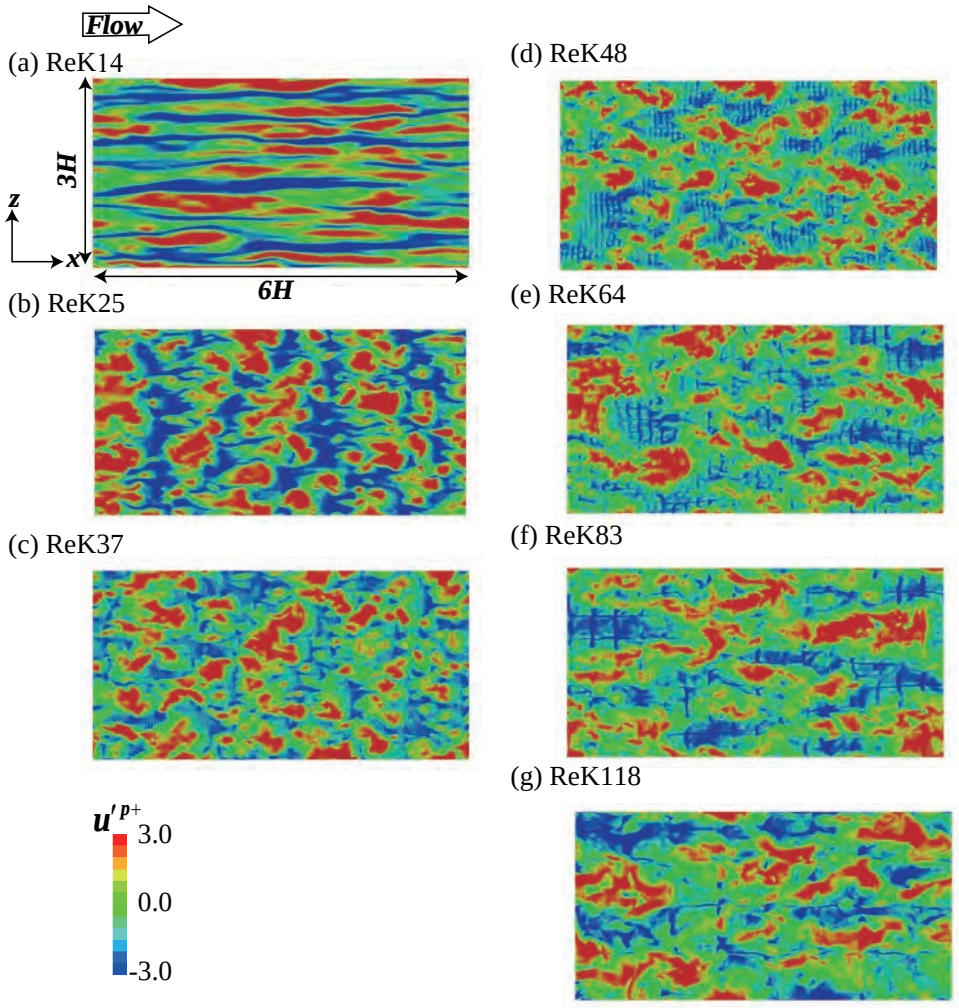

Figure 8: Snapshots of streamwise velocity fluctuations over the porous wall at $y'^{p+} \simeq 10$: (a) $\mathrm{Re}_K = 14$, (b) $\mathrm{Re}_K = 25$, (c) $\mathrm{Re}_K = 37$, (d) $\mathrm{Re}_K = 48$, (e) $\mathrm{Re}_K = 64$, (f) $\mathrm{Re}_K = 83$, and (g) $\mathrm{Re}_K = 118$.

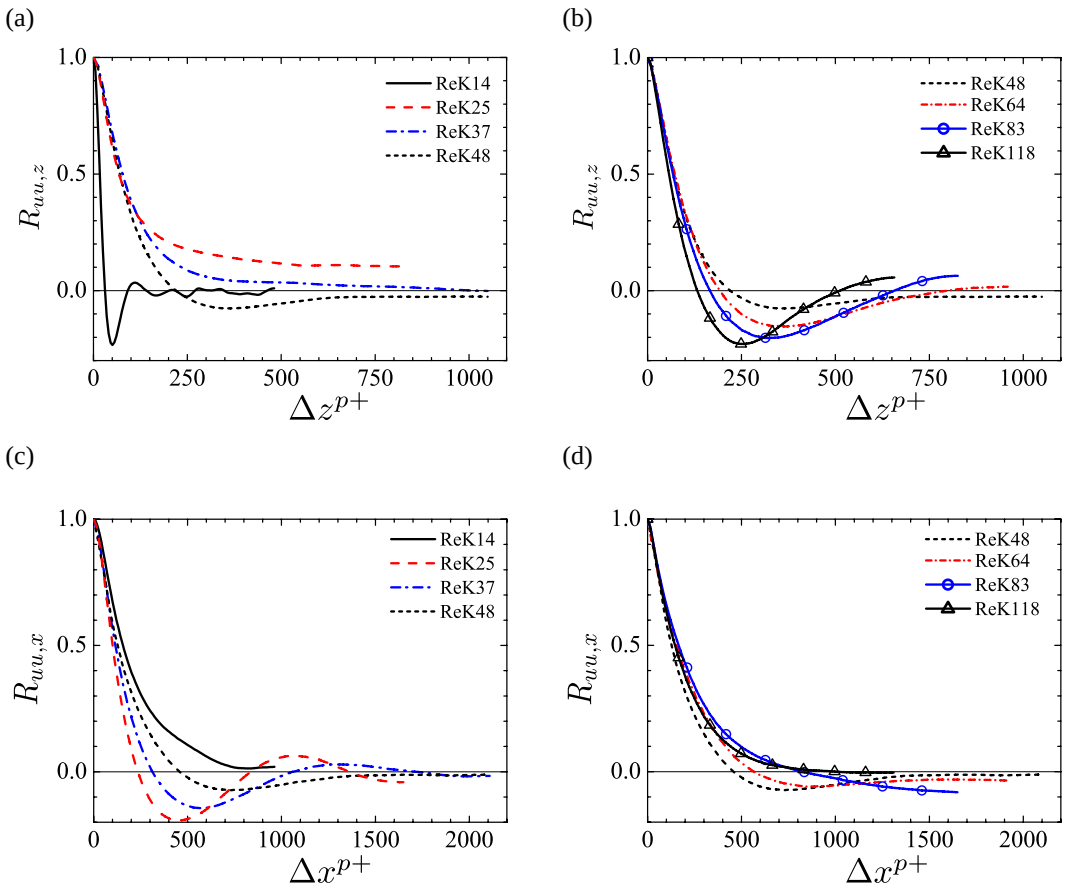

Figure 9: Two-point correlation functions along the streamwise and spanwise directions: (a) profiles of the spanwise correlation function $R_{uu,z}$ for $14 \leq \mathrm{Re}_K \leq 48$, (b) profiles of the spanwise correlation function $R_{uu,z}$ for $48 \leq \mathrm{Re}_K \leq 116$, (c) profiles of the streamwise correlation function $R_{uu,x}$ for $14 \leq \mathrm{Re}_K \leq 48$, and (d) profiles of the streamwise correlation function $R_{uu,x}$ for $48 \leq \mathrm{Re}_K \leq 116$.

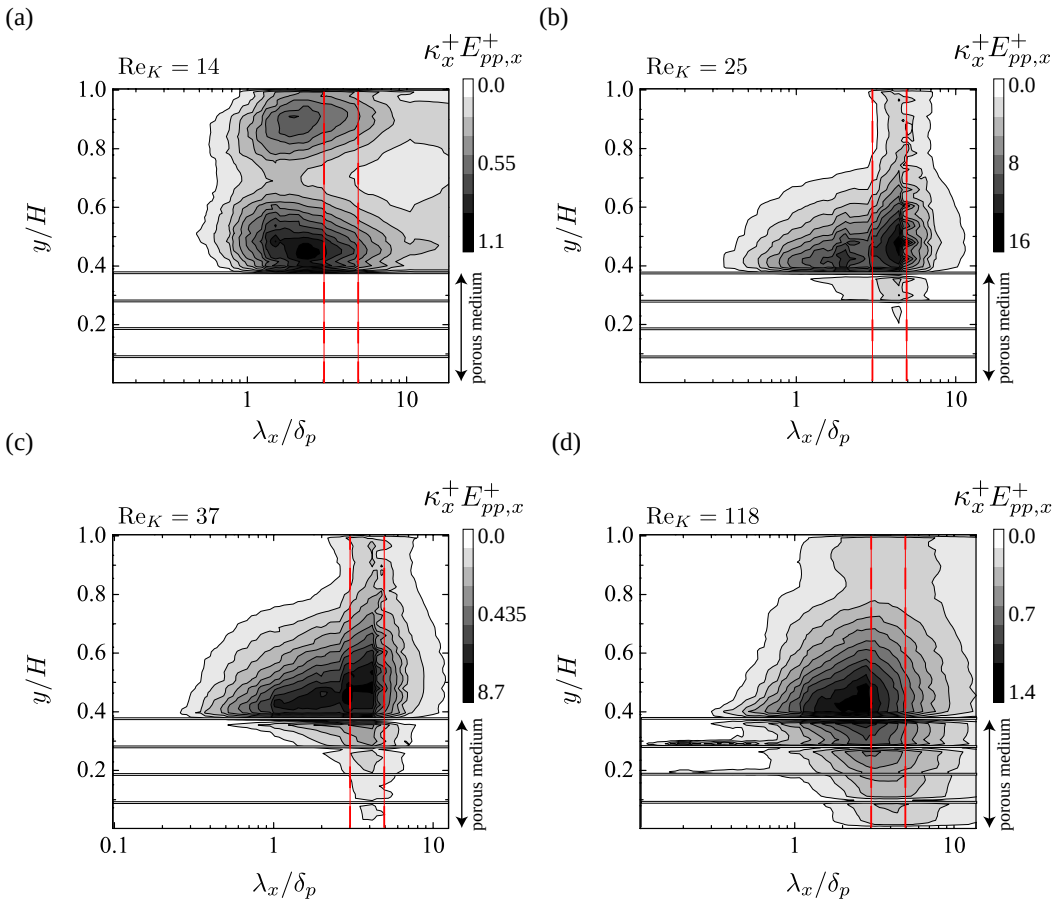

Figure 10: Contour maps of the wavenumber multiplied streamwise spectral energy density of pressure fluctuations $\kappa_x^+ E_{xx,p}^+$: (a) $\mathrm{Re}_K = 14$, (b) $\mathrm{Re}_K = 25$, (c) $\mathrm{Re}_K = 37$, and (d) $\mathrm{Re}_K = 116$; red broken lines indicate the position at $\lambda_x/\delta_p = 3$ and 4.

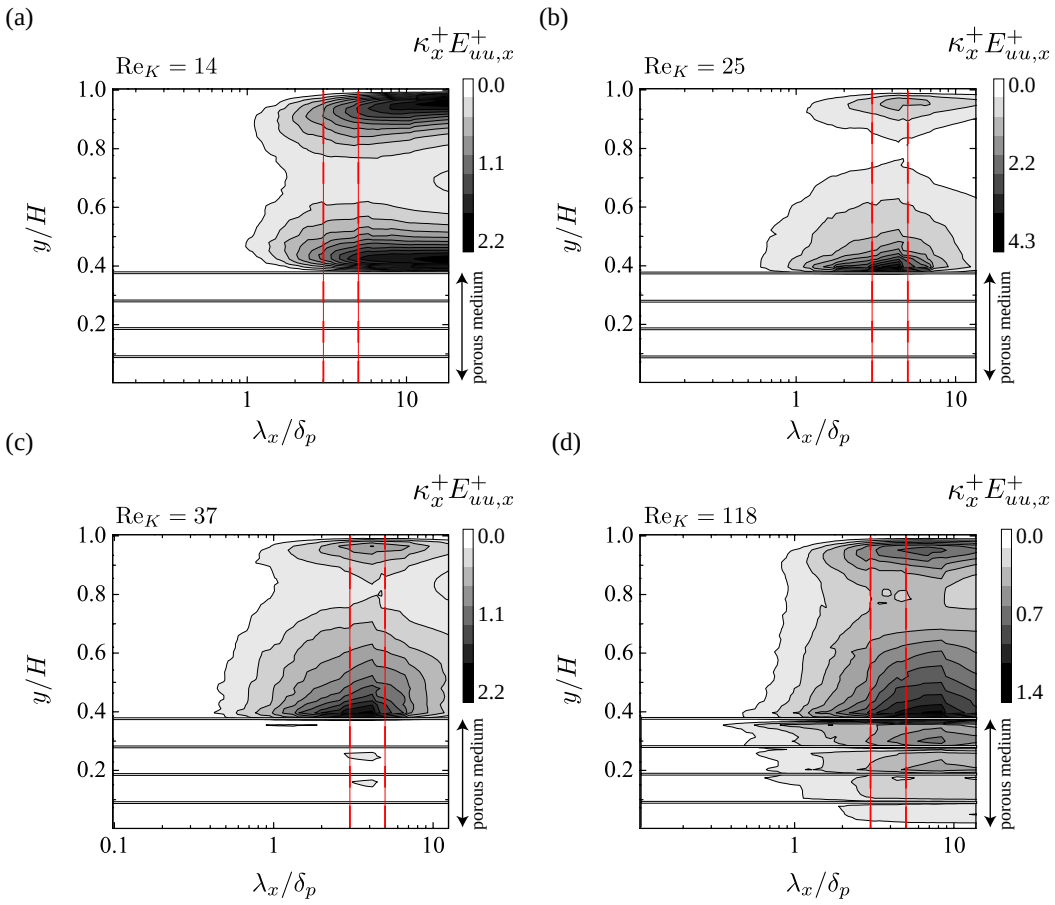

Figure 11: Contour maps of the wavenumber multiplied streamwise spectral energy density of streamwise velocity fluctuations $\kappa_x^+ E_{xx,u}^+$: (a) $\mathrm{Re}_K = 14$, (b) $\mathrm{Re}_K = 25$, (c) $\mathrm{Re}_K = 37$, and (d) $\mathrm{Re}_K = 116$; the red broken lines indicate the position at $\lambda_x/\delta_p = 3$ and 4.

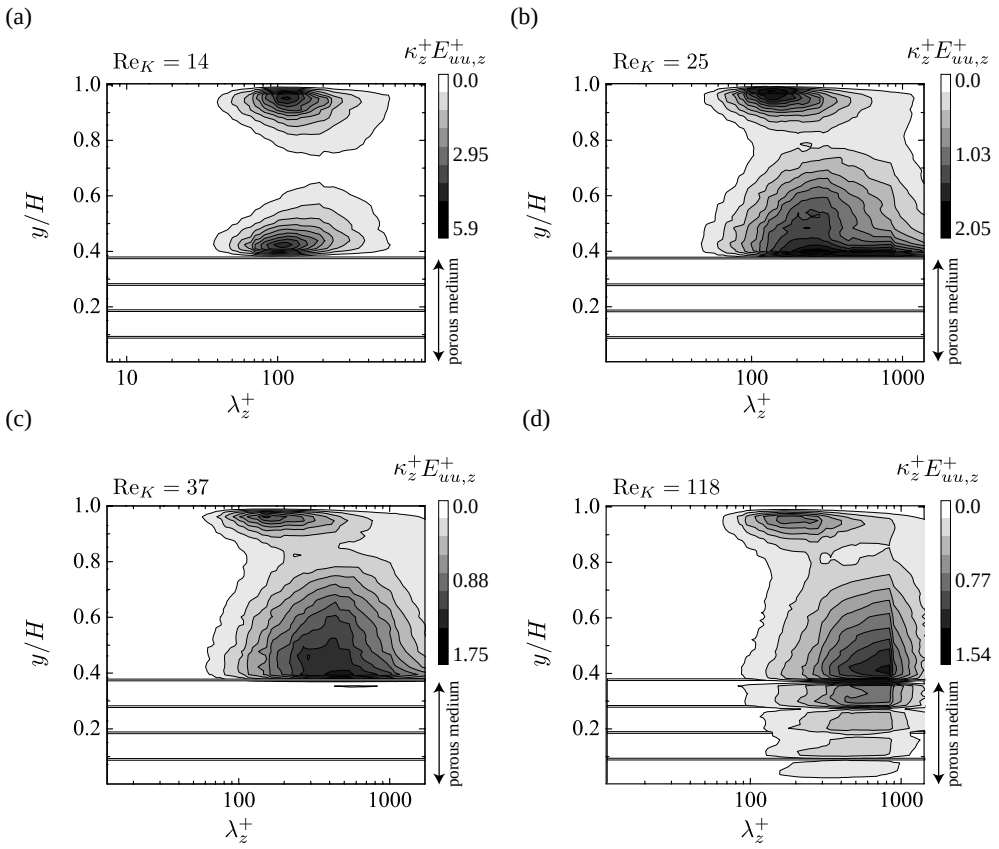

Figure 12: Contour maps of the wavenumber multiplied spanwise spectral energy density of streamwise velocity fluctuations $\kappa_z^+ E_{zz,u}^+$: (a) $\mathrm{Re}_K = 14$, (b) $\mathrm{Re}_K = 25$, (c) $\mathrm{Re}_K = 37$, and (d) $\mathrm{Re}_K = 116$.

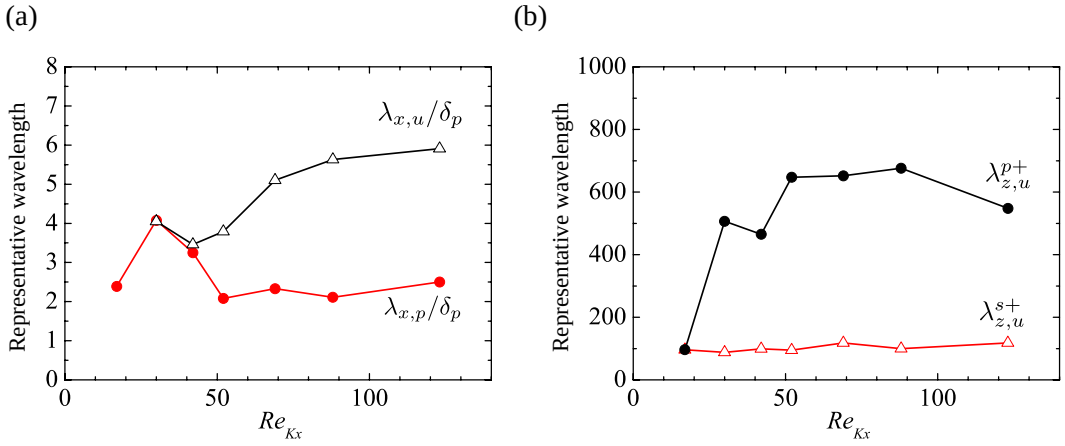

Figure 13: Representative wavelength of pressure and velocity fluctuations: (a) Variation of the streamwise representative wavelength of velocity fluctuations $\lambda_{x,u}$ and that of pressure fluctuations $\lambda_{x,p}$, both of which are normalised by the boundary layer thickness δ_p, and (b) Variation of the spanwise representative wavelength of velocity fluctuations over the porous wall $\lambda^{p+}_{z,u}$ and that below the solid wall $\lambda^{s+}_{z,u}$, both of which are normalised by their wall units.